Article

Defect-Rich Heterogeneous MoS₂/rGO/NiS Nanocomposite for Efficient pH-Universal Hydrogen Evolution

Guangsheng Liu [ID]**, Kunyapat Thummavichai** [ID]**, Xuefeng Lv, Wenting Chen, Tingjun Lin, Shipeng Tan, Minli Zeng, Yu Chen, Nannan Wang** *[ID] **and Yanqiu Zhu**

Guangxi Institute Fullerene Technology (GIFT), Guangxi Key Laboratory of Processing for Non-Ferrous Metals and Featured Materials, School of Resources, Environment and Materials, Guangxi University, Nanning 530004, China; Jesson_lgs@163.com (G.L.); kt302@exeter.ac.uk (K.T.); Betsy_Lv@163.com (X.L.); wt15578102973@126.com (W.C.); w15260260610@163.com (T.L.); 1739200127@st.gxu.edu.cn (S.T.); MinliZeng_97@163.com (M.Z.); yc465@exeter.ac.uk (Y.C.); Y.zhu@exeter.ac.uk (Y.Z.)
* Correspondence: Wangnannan@gxu.edu.cn

Abstract: Molybdenum disulfide (MoS₂) has been universally demonstrated to be an effective electrocatalytic catalyst for hydrogen evolution reaction (HER). However, the low conductivity, few active sites and poor stability of MoS₂-based electrocatalysts hinder its hydrogen evolution performance in a wide pH range. The introduction of other metal phases and carbon materials can create rich interfaces and defects to enhance the activity and stability of the catalyst. Herein, a new defect-rich heterogeneous ternary nanocomposite consisted of MoS₂, NiS and reduced graphene oxide (rGO) are synthesized using ultrathin αNi(OH)₂ nanowires as the nickel source. The MoS₂/rGO/NiS-5 of optimal formulation in 0.5 M H₂SO₄, 1.0 M KOH and 1.0 M PBS only requires 152, 169 and 209 mV of overpotential to achieve a current density of 10 mA cm⁻² (denoted as η_{10}), respectively. The excellent HER performance of the MoS₂/rGO/NiS-5 electrocatalyst can be ascribed to the synergistic effect of abundant heterogeneous interfaces in MoS₂/rGO/NiS, expanded interlayer spacings, and the addition of high conductivity graphene oxide. The method reported here can provide a new idea for catalyst with Ni-Mo heterojunction, pH-universal and inexpensive hydrogen evolution reaction electrocatalyst.

Keywords: electrocatalyst; hydrogen evolution reaction; molybdenum disulfide; reduced graphene oxide; nickel sulfide

1. Introduction

Hydrogen energy is expected to be an ideal energy source in the future due to its high energy density and zero pollution [1,2]. Electrolytic water is a simple and effective method to produce high purity hydrogen. High efficiency of hydrogen evolution reaction can be achieved by efficient electrocatalysts such as Pt, which can decrease the activated barrier and accelerate the reaction rate. However, noble electrocatalysts cannot be widely used in industrial hydrogen production because of their high price and scarcity. In view of the above, the development of high efficiency non-noble metal electrocatalysts is of great significance to boost the development of hydrogen energy resources.

Two-dimensional transition metal sulfides (TMDs), such as MoS₂, WS₂, NiS₂ and CoS₂, have been widely investigated due to their excellent electrocatalytic properties [3–6]. Among the materials, MoS₂ shows superior catalytic activity and is considered as a promising catalyst due to its low adsorption energy between unsaturated sulfur atoms and hydrogen atoms [7]. Unfortunately, few active sites, intrinsic low conductivity and insufficient stability hinder the HER activity of MoS₂ [8]. To solve these problems, various effective methods such as defect and interfaces engineering, structural design and elements doping technique have been introduced for improving electrocatalytic activity of

MoS_2. Considering that the active site was derived from the Mo-S of edge of MoS_2 catalysis, surface defects or interfaces are essential to improve the electrocatalytic activity of catalysts [9–11]. Various defect-rich MoS_2 electrocatalysts has been previously reported, including doping heteroatom to form various M-Mo-S (M = Co, Ni) structure [12–14], interlayer-expanded MoS_2 nanosheets [15], N-doped MoS_2 nanosheet [16] and addition of excessive sulfur sources [17]. These modified MoS_2 structures with poor crystallinity are easily dissolved in acidic solution, resulting in poor electrochemical stability. In addition, due to slow HER kinetics and poor stability in alkaline medium, it is still remaining a big challenge to produce MoS_2-based catalysts to meet the industrial requirements.

The kinetics of HER in acidic solution is 2–3 times faster than in alkaline solution due to the large adsorption energy of OH^- on the surface of catalyst in alkaline medium and high dissociation energy barrier between MoS_2 and water [18,19]. Modifying the MoS_2 structure helps to reduce its binding energy to hydroxyl, resulting in the improvement of catalyst HER performance in alkaline medium. Previous studies have demonstrated that NiS_x has excellent stability under alkaline conditions, and can form a heterostructure with MoS_2 nanosheets to achieve both high catalytic performance and play a protective role for MoS_2 [20].

Apart from HER performance, the charge conductivity of MoS_2-based catalyst is also another key performance for electrocatalytic materials. Nickel and copper foam materials have been used as conductive substrates and supporting materials, then in situ growth MoS_2 nanosheets on their surfaces [21–24]. This strategy has shown excellent performance in HER and OER processes. Unfortunately, the metal foam in these self-supporting catalysts could be dissolved by acid, which severely limits their widespread use. Carbon materials have excellent electrical conductivity and stability in a wide pH range, such as reduced graphene oxide (rGO), carbon fiber paper and carbon cloth. The reported CoS_2@MoS_2/rGO [19], MoS_2/rGO [25] and Mn/MoS_2/rGO [26] catalysts have good catalytic stability and electrocatalytic activity, which owes to the synergetic effect of rGO intrinsic high charge conduction characteristics [23]. Therefore, it is an effective strategy to grow MoS_2 on rGO using rGO as conductive substrate.

Herein, defect-rich multiphase MoS_2/rGO/NiS nanocomposite catalyst was successfully synthesized using $\alpha Ni(OH)_2$ nanowires with excellent catalytic performance and stability over a wide range of pH. The existence of abundant defects and heterogeneous interfaces was confirmed by X-ray diffraction analysis (XRD), Raman spectrum and high resolution transmission electron microscopy (HRTEM). Furthermore, the optimal MoS_2/rGO/NiS-5 nanocomposite exhibited very low overpotential and good stability in 0.5 M H_2SO_4 (η_{10} = 152 mV), 1.0 M KOH (η_{10} = 169 mV) and 1.0 M PBS (η_{10} = 209 mV), respectively.

2. Results and Discussion

The MoS_2/rGO/NiS nanocomposite with rich defects and heterogeneous interfaces was synthesized by two-step hydrothermal method, which is shown in Figure 1. (The detailed synthesized steps were in supporting information). L-cysteine hydrochloride (L-ch, $HSCH_2CHNH_2COOH \cdot HCl \cdot H_2O$) can conjugate well with graphene oxide (GO) due to its multifunctional groups (-SH, $-NH_2$, -COO). When heated, L-ch can not only be acted as a reductant to reduce Mo^{6+} to Mo^{4+}, but also expand the interlayer spacing of MoS_2 by releasing NH^{4+} and in situ intercalating into the interlayer of MoS_2. The $\alpha Ni(OH)_2$ adsorbed on the GO was sandwiched between the GO and the MoS_2 nanosheets and was vulcanized into NiS, while the GO was also in situ reduced to reduced graphene oxide (rGO) during the hydrothermal process. Furthermore, the weakly acidic conditions formed by the dissolution of L-ch can dissolve a small amount of $\alpha Ni(OH)_2$ and reduce the dissolved Ni^{2+} to Ni^0 and then dope it into MoS_2.

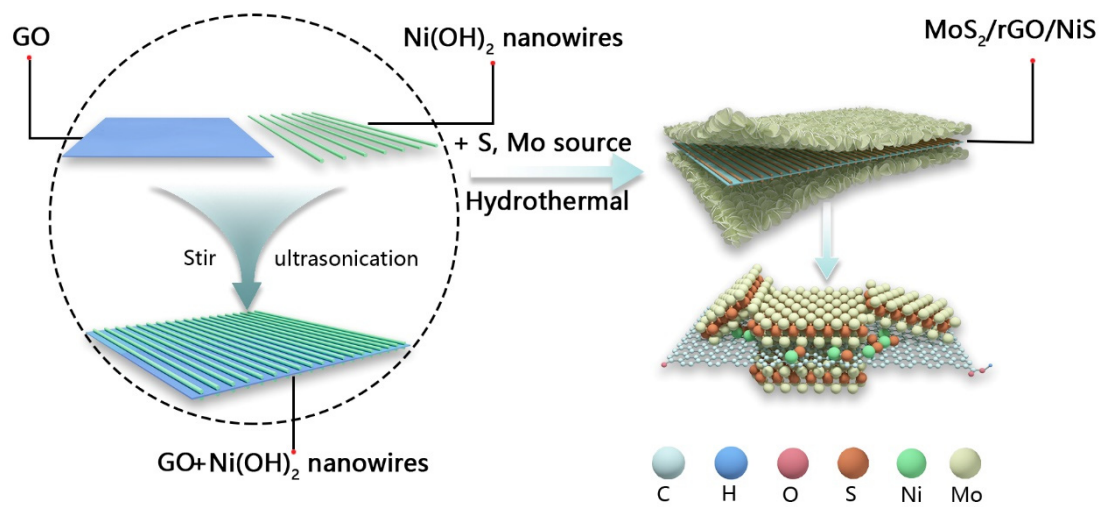**Figure 1.** Schematic of synthesized process and structural of MoS_2/rGO/NiS-X (where X is the volume of $\alpha Ni(OH)_2$ added, X = 0, 3, 5, 7).

The crystal phases change of MoS_2 based samples before and after doping GO and $\alpha Ni(OH)_2$ are shown in Figure 2a. The diffraction peaks at 33.76°, 35.12° and 57.76°, correspond to (101), (102) and (110) plane of 2H-MoS_2 (JPCDS no. 37-1492), respectively. These peaks are broad, indicative of the poorly crystallization of the samples. The standard (002) peak of pristine 2H-MoS_2 at 14.4° are not observed in our as-prepared MoS_2 samples. Instead, a peak at 9.41° is obtained, which can be ascribed to the insertion of NH^{4+} into MoS_2 structure, suggesting an enlarged d value [27]. According to Bragg's Law (nλ = 2dsinθ), the spacing between two adjacent S-Mo-S layers are calculated to be about 0.94 nm [28,29]. The (002) diffraction peak of the MoS_2/rGO/NiS-5 shifts toward the lower 2-theta position at 8.5° compare with as-prepared MoS_2. The d value is also calculated to be 1.06 nm, in accordance well with the results of TEM (Figure 3e). The reason of (002) peak shift is that graphene oxide may inhibit the growth of MoS_2 crystal in the mixed catalyst. The diffraction pattern of MoS_2/rGO/NiS-5 catalyst also matched well with NiS standard pattern (JCPDS no. 02-1280), suggesting $\alpha Ni(OH)_2$ was transformed into NiS. Four broad peaks of NiS located at 30.37°, 34.65°, 45.70° and 53.93° were attributed to (100), (101), (102) and (110) planes, respectively. The XRD spectrum of $\alpha Ni(OH)_2$ nanowires is shown in Figure S1a.

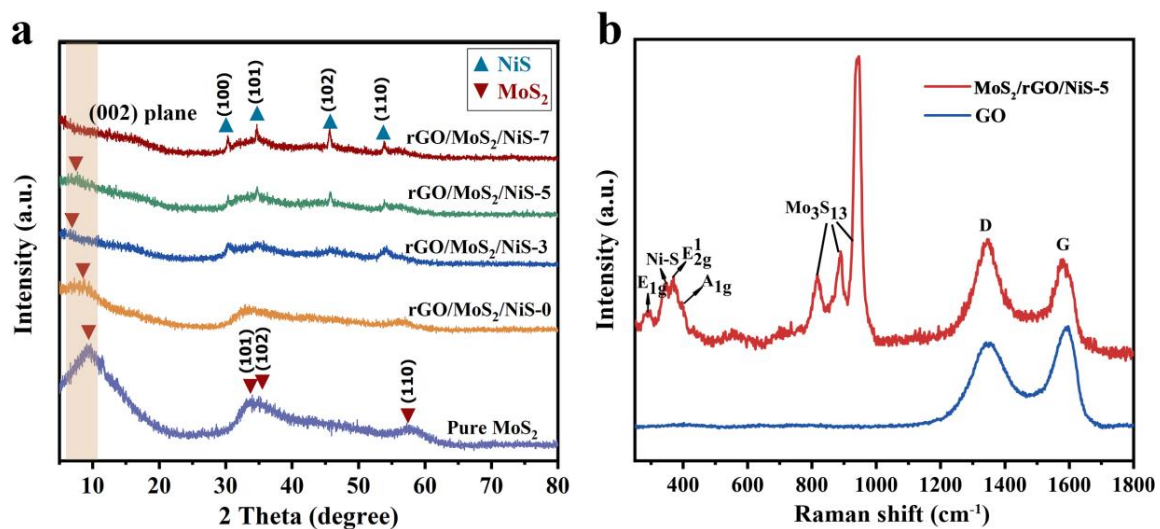**Figure 2.** (**a**) XRD patterns of MoS_2/rGO/NiS-X (X = 0, 3, 5, 7) nanocomposite and pure MoS_2 (**b**) Raman spectrum of MoS_2/rGO/NiS-5 nanocomposite and GO.
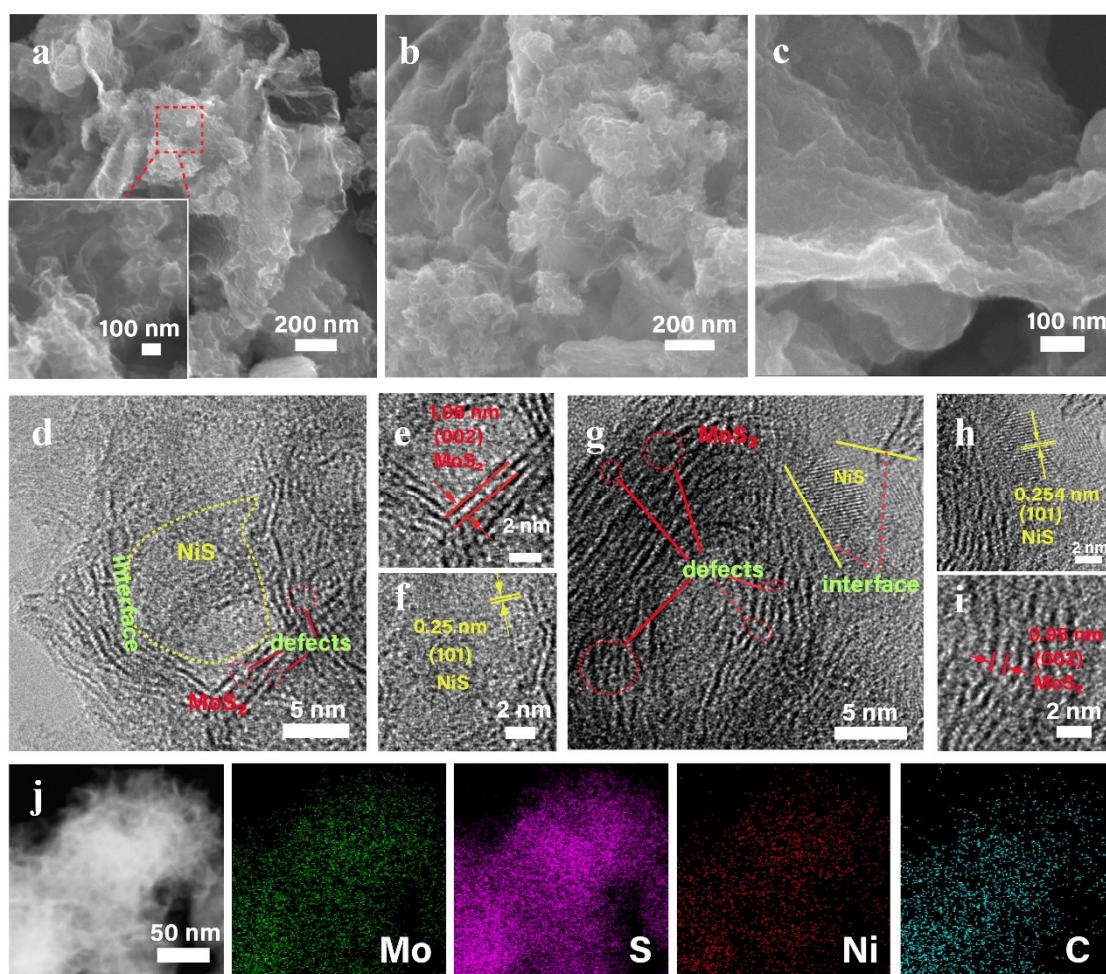
Figure 3. (**a–c**) SEM images of MoS$_2$/rGO/NiS-5 nanocomposite. (**d–i**) HRTEM images of MoS$_2$/rGO/NiS-5 nanocomposite. (**j**) HAADF-STEM and corresponding element mapping images in MoS$_2$/rGO/NiS-5 nanocomposite.

Furthermore, the structural characteristics of the MoS$_2$/rGO/NiS-5 can be obtained from the Raman spectrum in Figure 2. The main peaks at ~402, ~371 and ~296 cm^{-1} are attributed to A^1_g, E$^1_{2g}$ and E^1_g mode of 2H MoS$_2$, respectively, whereas the peak located at ~345 cm^{-1} belong to the modes of Ni-S [30,31]. More importantly, three sharp peaks in the range of 800–1000 cm^{-1} originate from the molecular structure of Mo$_3$S$_{13}$ located at edge of MoS$_2$. It can be proven that there are abundant unsaturated Mo-S edge sites in MoS$_2$/rGO/NiS-5 [19,30]. There are two characteristic peaks at ~1437 and ~1580 cm^{-1}, which are G and D-band of GO, respectively. The degree of graphitization can be expressed by the strength ratio of D and G bands. As shown in Figure 2b, the I$_D$/I$_G$ of MoS$_2$/rGO/NiS-5 (value of 1.11) is higher than that of GO (value of 0.83), indicating that the defects of GO increase with the reduction of oxygen-containing functional groups and GO is transformed into rGO [4,32].

Large specific surface area is a critical factor to determine the performance of the electrocatalyst of the electrode materials for the HER. The N$_2$ isothermal adsorption desorption curve of the MoS$_2$/rGO/NiS-5 shows type-IV isotherm (Figure S2), suggesting the existence of both micro-pores and meso-pores [33]. This specific surface area was 20.7 m^2 g^{-1}, which benefits from the abundant MoS$_2$ nanosheets wrinkles and small particle size. The morphology of the MoS$_2$/rGO/NiS-5 was shown in Figures 3 and S3. A large number of as-prepared αNi(OH)$_2$ nanowires are anchored uniformly on the GO substrate (Figure S1d). It is observed that the MoS$_2$/rGO/NiS-5 has a 3D crimp structure, which is attributed to the GO curling during hydrothermal process [34]. A large number of ultra-thin MoS$_2$ nanosheets suspended on rGO are presented in Figures 3a–c and S3a,b. Such microstructure

is conducive to exposing more marginal catalytic active sites. Further, the TEM images in Figure S3c prove that the microstructure of the nanowires is maintained after the αNi(OH)$_2$ nanowires are vulcanized to NiS. Moreover, the hybrid catalyst has a three-dimensional structure consisting of three layers of rGO, NiS and MoS$_2$. The HRTEM image exhibited lattice fringe with spacing of 1.06 and 0.95 nm, which belonged to the (002) plane of MoS$_2$ (Figure 3e,i). The lattice fringe of ~0.25 nm is indexed to the (101) plane of NiS (Figure 3f,h). Heterogeneous interface between MoS$_2$ and NiS are observed (Figure 3d,g), resulting in rich-defects and disordered structure of our samples. Furthermore, the element mapping of the MoS$_2$/rGO/rGO/NiS-5 hybrid sample is also carried out, which proves that Mo, Ni and S elements are uniformly distributed on rGO nanosheets (Figure 3j). The elemental composition ratio and spectral pattern of the hybrid catalyst are presented in Figure S3.

The chemical states of elements in MoS$_2$/rGO/NiS-5 nanocomposite were investigated by XPS. The survey XPS spectrum shows that the samples contain Mo, S, Ni, C, O, and N elements in Figure S4a, which is verified by the results of EDS. From the percentage of atomic orbital, it can be known that 27.39% S 2p bonding with 13.85% Mo 3d and 3.36% Ni 2p orbitals (Figure S4), which indicates the existence of Mo-S defects. Comparing C 1s spectrum in GO sheets and MoS$_2$/rGO/NiS-5 nanocomposite, the two peaks in GO at 286.7 eV and 287.5 eV are ascribed to graphitic sp^2 carbon atom and C=O (Figure S4b) [4,35,36]. However, these two peaks disappeared after hydrothermal treatment, which suggests that some of the oxygen-containing functional groups were reduced (Figure 4a). A new peak of C=N in C 1s spectrum of MoS$_2$/rGO/NiS-5 appeared at 285.8 eV, which could be due to the part of NH^{4+} released by L-ch doping for rGO [37,38]. Two main Mo 3d peaks at 228.9 eV and 232.1 eV correspond to 3d$_{5/2}$ and 3d$_{3/2}$ of Mo^{4+}, respectively, affirming the dominance of Mo^{4+} in MoS$_2$/rGO/NiS-5 nanocomposite (Figure 4b). Another doublet peak is detected at 233.0 and 235.63 eV, which ascribe to the oxidation state of Mo^{4+}. The peak of S 2s at 226.2 eV indicates the formation of Mo-S and Ni-S bonds [33,39]. For S 2p spectrum (Figure 4c), two types of distinct doublets (2P$_{3/2}$, 2P$_{1/2}$) were examined: (1) the peaks at 161.8 eV and 163.4 eV are divided and fitted to S 2p$_{3/2}$ and S 2p$_{1/2}$, respectively. (2) Another doublet at 162.9 and 164.5 eV are attributed to the bridging S$_2^{2-}$ ligands and the apical S^{2-} ligand of the [Mo$_3$S$_{13}$]$^{2-}$, in agreement with the result of Raman spectrum [26,37,40]. Two resolved doublets (with a spin-orbits splitting of ~17.3 eV between 2p$_{3/2}$ and 2p$_{1/2}$) and two satellites are observed in the spectrum of Ni 2p (Figure 4d). The peaks located at 853.6 eV and 870.9 eV correspond to metallic Ni^0 species in the sample; hence, the existence of Ni^0 could be due to the reducibility of L-ch. The other two peaks at 856.0 and 873.7 eV in the spectrum are attributed to the presence of Ni^{2+} component [41,42].

The HER activity of the hybrid catalysts was investigated in different pH electrolyte solutions including 0.5 M H$_2$SO$_4$, 1.0 M KOH and 1.0 M PBS. Commercial 20% Pt/C was also examined in different electrolyte solutions. In acidic medium, the electrode coated with pristine MoS$_2$ showed the worst catalytic activity, as shown in Figure 5a. Both MoS$_2$/NiS-5 and MoS$_2$/rGO/NiS-0 samples were exhibited higher catalytic activity and lower overpotential than the pristine MoS$_2$. Hence, the trend of catalytic currents for these doped catalysts is MoS$_2$/rGO/NiS-0 > MoS$_2$/NiS-5 > MoS$_2$. After adding different amounts of αNi(OH)$_2$ into the MoS$_2$/rGO, the activity increased with the increase of αNi(OH)$_2$, whereas the activity decreased when the addition amount of αNi(OH)$_2$ reached 7 mL. The optimal MoS$_2$/rGO/NiS-5 exhibits excellent catalytic performance (η_{10} = 152 mV) and requires only 212 mV overpotential to achieve a current density of 100 mA cm^{-2} (denoted as η_{100}) in acidic medium. Interestingly, when the current density is smaller than 40 mA cm^{-1}, the polarization curves of MoS$_2$/rGO/NiS-0 and MoS$_2$/rGO/NiS-3 almost coincide. However, when the current density is more than 40 mA cm^{-2}, the overpotential of MoS$_2$/rGO/NiS-0 is larger than that of MoS$_2$/rGO/NiS-3, which is probably because formed NiS improves the stability of MoS$_2$. The overpotential of the MoS$_2$/rGO/NiS-7 (η_{10} = 241 mV) is larger than other doped catalysts, which may be due to the fact that the large amount of NiS covers the active site of MoS$_2$.
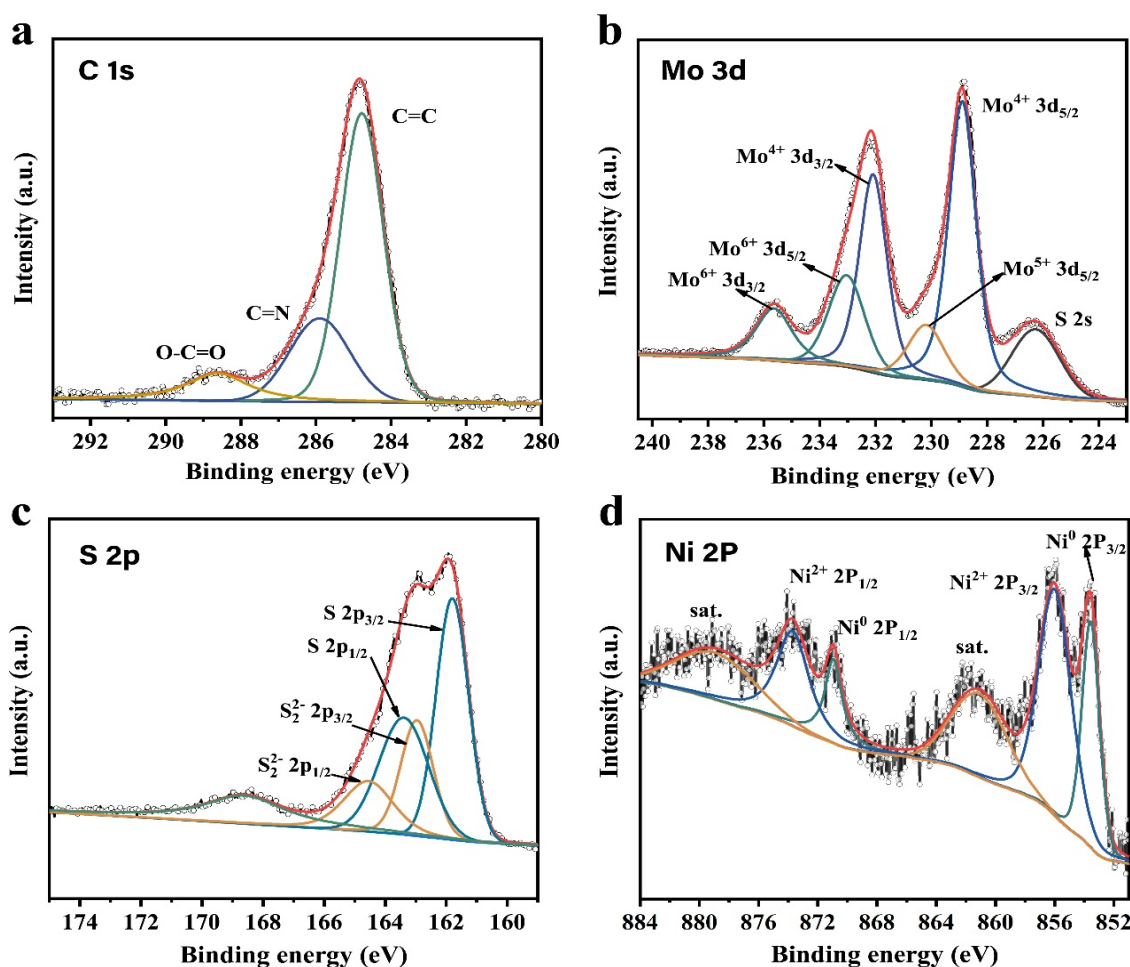
Figure 4. XPS spectra of (**a**) C 1s, (**b**) Mo 3d, (**c**) S 2p, and (**d**) Ni 2p in MoS_2/rGO/NiS-5 nanocomposite.

The MoS_2/rGO/NiS-5 exhibits the best HER catalyst activity under alkaline condition, and the overpotential are 169 and 301 mV at current density of 10 and 100 mA cm^{-2}, respectively (Figure 5d). Different from acid medium, the overpotential MoS_2/rGO/NiS-7 exhibits the second lowest overpotential in alkaline media (η_{10} = 357 mV), which is related to the heterogeneous interface between NiS and MoS_2 that facilitates the dissociation of water molecules. In neutral condition, the overpotential of MoS_2/rGO/NiS-5 showed modest overpotential at 10 mA cm^{-2} (η_{10} = 209 mV) (Figure 5g).

The Tafel slope was fitted from the LSV curve to evaluate the HER kinetics of as-prepared samples. In 0.5 M H_2SO_4 (Figure 5b), MoS_2/rGO/NiS-5 showed a very small Tafel slope of 54.3 mV/dec, which is close to 32.2 mV/dec of Pt/C. The small Tafel slope indicating that the HER first occur a very fast Volmer step ($H_3O^+ + e^- \rightarrow H_{ads} + H_2O$), followed by a slow electrochemical desorption Heyrovsky step ($H_{ads} + H_3O^+ + e^- \rightarrow H_2 + H_2O$), and the desorption reaction of hydrogen was the rate limiting step of HER [38,43,44]. Moreover, the Tafel slopes for MoS_2/rGO/NiS-X (X = 0, 3, 5, 7) and Pt/C were 190.4, 186.4, 91.6, 150.1 and 58.3 mV/dec in 1.0 M KOH solution, respectively (Figure 5e). The lower Tafel slope of MoS_2/rGO/NiS-5 indicates the Volmer-Heyrovsky recombination mechanism of HER and the Volmer step of water splitting into protons and hydroxyls is the main step determining the reaction rate [45]. In 1.0 M PBS, the Tafel slopes of MoS_2/rGO/NiS-X and Pt/C were 354.8, 215.7, 141.9, 216.3 and 69.7 mV/dec, respectively (Figure 5h). The results revealed that the rate limiting step of HER for as-prepared samples is slow Volmer step in a neutral medium [44].
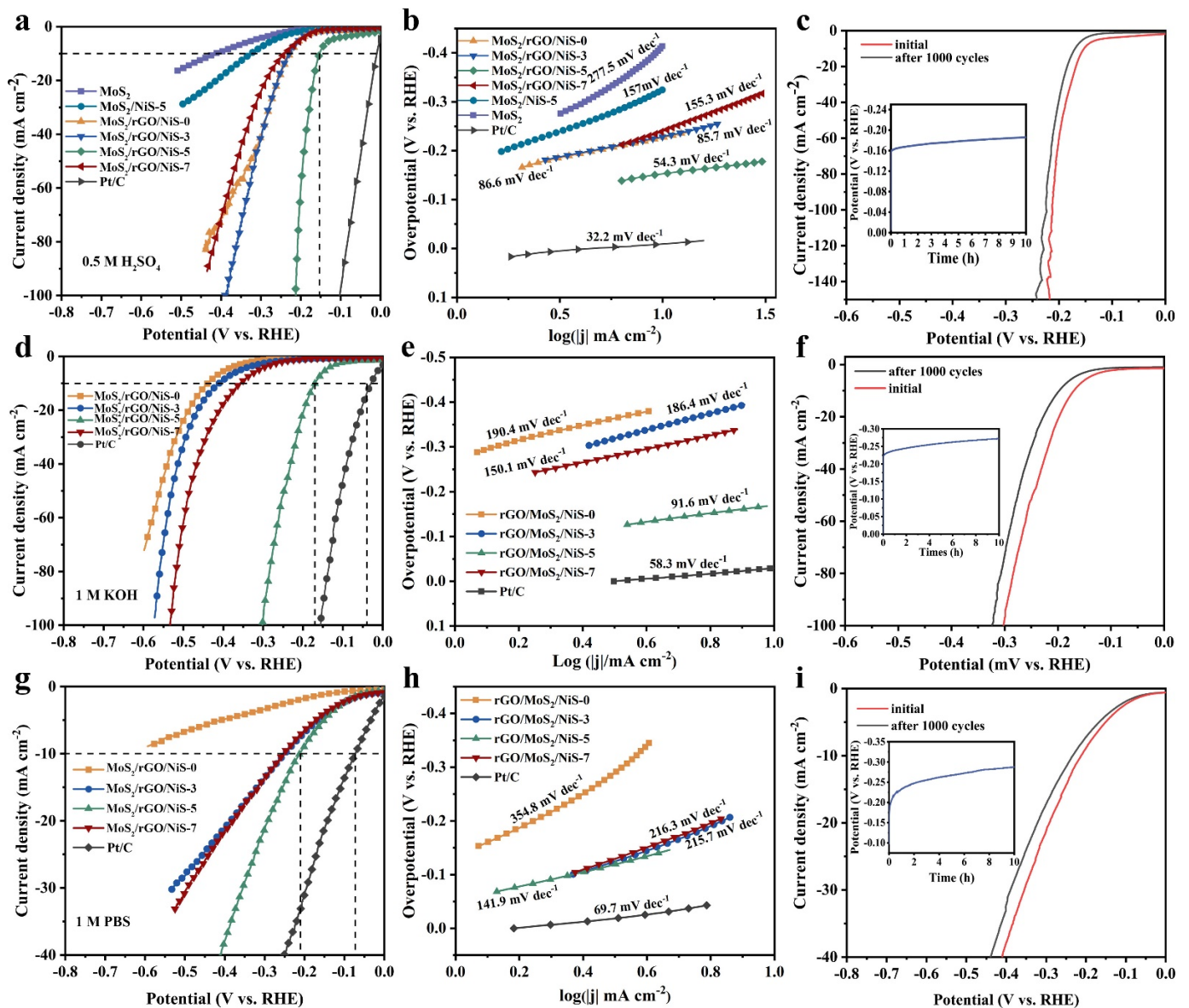
Figure 5. HER catalytic activities of the as-prepared samples. (**a**,**d**,**g**) Polarization curves in 0.5 M H_2SO_4, 1.0 M KOH and 1.0 M PBS, respectively. (**b**,**e**,**h**) Tafel plots under 0.5 M H_2SO_4, 1.0 M KOH and 1.0 M PBS, respectively. (**c**,**f**,**i**) The polarization curves of MoS_2/rGO/NiS-5 before and after 1000 cycles of voltammetry in 0.5 M H_2SO_4, 1.0 M KOH and 1.0 M PBS were compared, respectively. Their insets were chronopotentiometric curves under 0.5 M H_2SO_4, 1.0 M KOH and 1.0 M PBS, respectively.

The MoS_2/rGO/NiS-5 nanocomposite suggests excellent stability in acidic, alkaline and neutral medium, as the polarization curve after 1000 cycles (Figure 5c,f,i), in which the overpotential has only increased by 17, 27 and 23 mV, respectively. Furthermore, chronopotentiometry of catalyst in different media were performed under 10 mA cm^{-2} current density of for 10 h (as shown in the insets image of Figure 5c,f,i). After ten hours, the overpotential increased by 14.4% (from 163 to 186 mV), 20.8% (from 226 to 273 mV) and 37.9% (from 208 to 287 mV) in 0.5 M H_2SO_4, 1.0 M KOH and 1.0 M PBS, respectively. These results indicate that the as-prepared MoS_2/rGO/NiS-5 has a good stability, and it is more stable under acidic conditions than in alkaline and neutral conditions. Compared with other MoS_2-based electrocatalysts reported recently, the MoS_2/rGO/NiS-5 has superior performance in acidic and alkaline media (Table 1).

Table 1. Comparison of the MoS$_2$-based catalyst in acidic and alkaline electrolytes.

Catalysts	Medium	η(mV) [a]	Tafel Slope (mV/dec)	Loading (mg/cm^{-2})	Substrate	Ref.
MoS$_2$/rGO/NiS	0.5 M H$_2$SO$_4$	152	54.3	0.353	GC	this work
Ag$_2$S/MoS$_2$/rGO	0.5 M H$_2$SO$_4$	190	56.0	0.250	GC	[44]
MoN-MoS$_2$	0.5 M H$_2$SO$_4$	190	59	0.250	GC	[46]
CoS$_2$-C@MoS$_2$	0.5 M H$_2$SO$_4$	173	61	0.250	GC	[47]
Ag$_2$S/MoS$_2$	0.5 M H$_2$SO$_4$	220	42	0.570	GC	[25]
N-C/MoS$_2$	0.5 M H$_2$SO$_4$	185	57	0.105	GC	[38]
MoS$_2$/rGO/NiS	1 M KOH	169	91.6	0.353	GC	this work
MoSx@NiO	1 M KOH	406	43	0.706	GC	[48]
MoS$_2$@FePS$_3$	1 M KOH	175	127	2.000	NF [b]	[49]
Co$_9$S$_8$@MoS$_2$	1 M KOH	177	83.6	——	GC	[50]
Co$_3$S$_4$/MoS$_2$/Ni$_2$P	1 M KOH	178	98	0.510	GC	[51]
MoS$_2$/rGO	1 M KOH	168	83.9	0.566	GC	[52]

[a] Overpotential at a current density of 10 mA/cm^2. [b] Nickel foam.

The electrochemical double-layer capacitance (C$_{dl}$) of as-synthesized catalysts was measured to evaluate the electrochemical active surface areas (ECSA). Cyclic voltammograms (CVs) with various scan rates from 40–200 mV s^{-1} (Figures S5–S7) were recorded to calculate C$_{dl}$. The capacitance current ($\Delta j = j_a - j_c$) and the scanning rates are fitted into a straight line, and the slope of the line is twice the value of C$_{dl}$. The slope of MoS$_2$/rGO/NiS-X (X = 0, 3, 5, 7) are 7.1, 9.01, 11.9 and 4.58 mF cm^{-2} in 0.5 M H$_2$SO$_4$, respectively (Figure 6a). Notably, MoS$_2$/rGO/NiS-5 with the highest C$_{dl}$ (5.95 mF cm^{-2}) has the largest ECSA compared to other samples, which further demonstrates its excellent HER performance in acidic medium. The MoS$_2$/rGO/NiS-5 (C$_{dl}$ = 2.76 mF cm^{-2}) exhibits better HER performance than MoS$_2$/rGO/NiS-7 (C$_{dl}$ = 2.46 mF cm^{-2}) despite that they have similar ECSA in the alkaline medium (Figure 6c), indicating that the catalytic activity is determined by the coordination of hydrogen adsorption and the active sites of water adsorption/dissociation [46]. Similarly, MoS$_2$/rGO/NiS-5 still has the largest C$_{dl}$ value (1.66 mF cm^{-2}) in neutral media (Figure 6e).

Electrochemical impedance spectra (EIS) was measured to further investigate the charge-transfer kinetics between electrocatalysts and electrolyte interface (Figure 6b,d,f). The EIS data are fitted to acquire the equivalent circuit patterns (insets in Figure 6b,d,f), where R$_s$ is the solution resistance, the R$_c$ at the high frequency region is related to the pores on the material surface and does not change with the change of overpotential, and the R$_{ct}$ at the low frequency region represents the charge transfer impedance [43]. The results of the fitting data are shown in Tables S1–S3. Evidently, MoS$_2$/rGO/NiS-5 shows the lowest charge transfer resistance value of 19.75, 14.3 and 105.1 ohm in acidic, alkaline and neutral electrolytes, which demonstrate it's the high electrochemical conductivity. Simultaneously, it can be clearly seen that the R$_{ct}$ of MoS$_2$/rGO/NiS-X in acid solution is much smaller than that of MoS$_2$/NiS-5 (515.2 ohm), which is because the addition of rGO enhances the rate of electrons transfer between the electrode and catalytic active site. Furthermore, experiments show that 5 mL of αNi(OH)$_2$ is the best addition to reduce the impedance of the catalyst. Importantly, the results of EIS studies are in agreement with above results of electrochemical performances studies. These results also confirmed that the abundant heterogeneous interface between NiS and MoS$_2$ allow not only to expose dense catalytic sites but also improves the electron transfer ability of catalytic materials, which further enhance the catalytic activity of electrocatalyst.
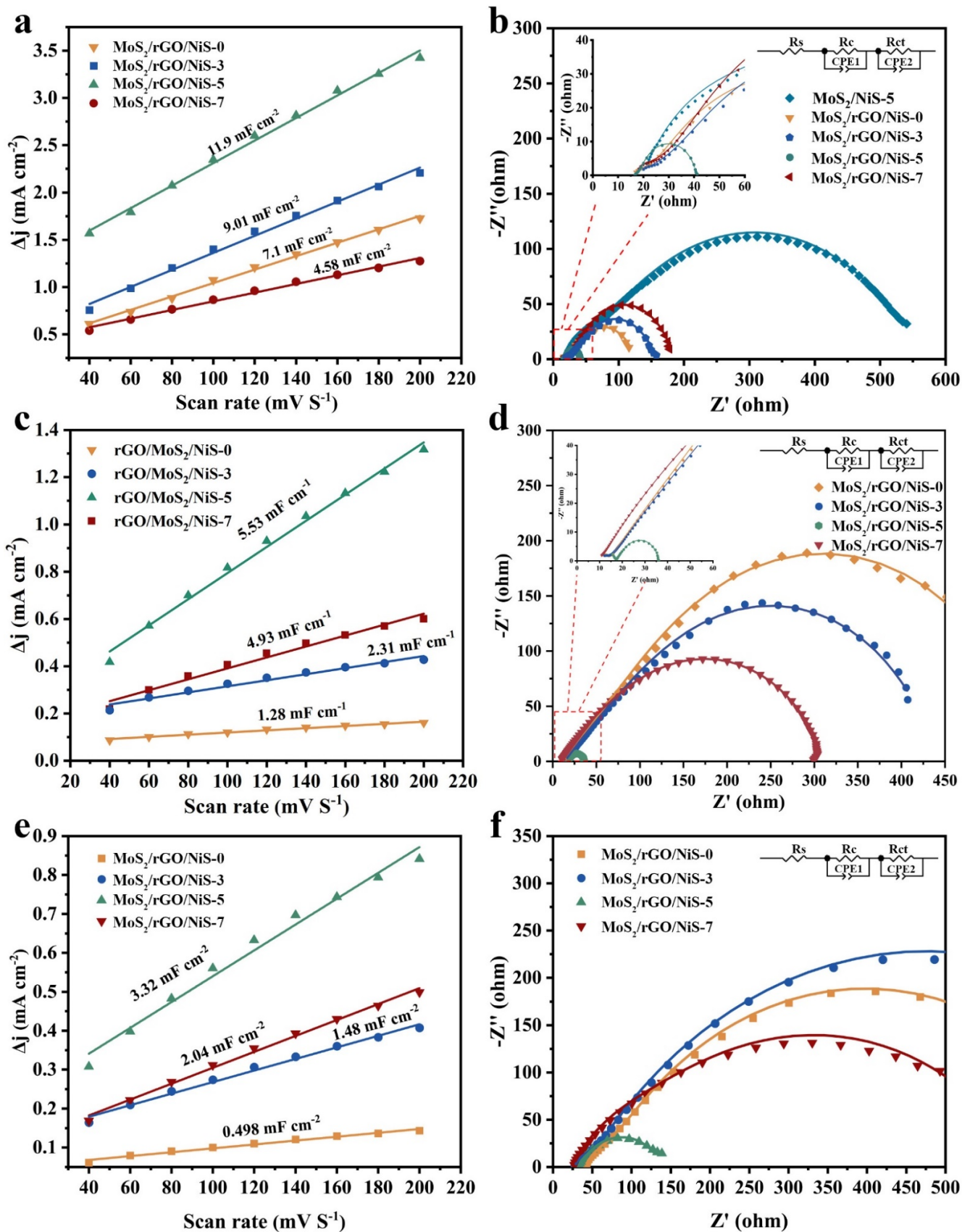
Figure 6. Calculated double-layer capacitance for the samples in (**a**) 0.5 M H_2SO_4, (**c**) 1.0 M KOH and (**e**) 1.0 M PBS. The Nyquist plots (solid lines), fitting data (dot) and equivalent circuit (inset) of the samples in (**b**) 0.5 M H_2SO_4, (**d**) 1.0 M KOH and (**f**) 1.0 M PBS.

3. Conclusions

In this paper, defect-rich heterogeneous MoS_2/rGO/NiS nanocomposite for HER has been successfully synthesized using $\alpha Ni(OH)_2$ nanowires with excellent catalytic performance and stability over a wide range of pH. The effect of different amounts of NiS on the HER activity of MoS_2/rGO were investigated. The results confirmed that defect-rich heterogeneous MoS_2/rGO/NiS can be used as an efficient and stable HER catalyst under a universal range of pH electrolyte condition. The optimal MoS_2/rGO/NiS-5 electrocatalysts exhibited good stability as well as very low overpotential in 0.5 M H_2SO_4 (η_{10} = 152 mV), 1.0 M KOH (η_{10} = 169 mV) and 1.0 M PBS (η_{10} = 209 mV), respectively. The outstanding HER performance of MoS_2/rGO/NiS-5 catalyst can be ascribed mainly to the following three points: (1) the abundant heterogeneous interface between NiS and MoS_2 can expose dense catalytic sites and accelerate electron transfer, which synergistically promotes electrocatalytic activity in a wide pH range; (2) the enlarged interlayer spacing of MoS_2 exposes more marginal active edge sites; (3) the high intrinsic conductivity of rGO facilitates the rate of charges transfer between electrode and active catalytic site. This work can provide a new idea for designing Ni-Mo heterojunction materials as an efficient and low-cost pH-universal HER electrocatalyst.

Supplementary Materials: The following are available online at https://www.mdpi.com/2079-4991/11/3/662/s1, Figure S1: (a) XRD spectrum, (b) TEM images and (c) SEM images of $\alpha Ni(OH)_2$ nanowires; (d) SEM image of $\alpha Ni(OH)_2$ adsorbed on GO, Figure S2: N_2 adsorption-desorption isotherms and the corresponding pore size-distribution profiles of MoS_2/rGO/NiS-5, Figure S3: (a–c) Low magnification TEM images and (d) TEM-EDS pattern of MoS_2/rGO/Ni-5, Figure S4: (a) The survey XPS spectrum of MoS_2/rGO/NiS-5; (b) XPS spectrum of C 1s of GO, Figure S5: (a–d) Cyclic voltammograms curves of the MoS_2/rGO/NiS-X (X = 0, 3, 5, 7) in 0.5 M H_2SO_4 under 0.36–0.46 V vs. RHE, Figure S6: (a–d) Cyclic voltammetry curves of the MoS_2/rGO/NiS-X (X = 0, 3, 5, 7) in 1 M KOH under 0.6–0.7 V vs. RHE, Figure S7: Cyclic voltammetry curves of the MoS_2/rGO/NiS-X (X = 0, 3, 5, 7) in 1 M PBS under 0.7–0.8 V vs. RHE. Table S1: The electrochemical impedance fitting results of as-prepared samples in 0.5 M H_2SO_4, Table S2: The electrochemical impedance fitting results of as-prepared samples in 1 M KOH, Table S3: The electrochemical impedance fitting results of the prepared samples in 1 M PBS.

Author Contributions: Conceptualization, G.L., K.T., and X.L.; writing-original draft preparation, G.L., W.C., T.L., and Y.C.; experiment, S.T. and M.Z.; funding acquisition, N.W., Y.Z. All authors have read and agreed to the published version of the manuscript.

Conflicts of Interest: The authors declare no conflict of interest.

References

1. Zhao, J.; Li, Y.; Yang, G.; Jiang, K.; Lin, H.; Ade, H.; Ma, W.; Yan, H. Efficient organic solar cells processed from hydrocarbon solvents. *Nat. Energy* **2016**, *1*, 15027. [CrossRef]
2. Huang, Y.; Sun, Y.; Zheng, X.; Aoki, T.; Pattengale, B.; Huang, J.; He, X.; Bian, W.; Younan, S.; Williams, N. Atomically engineering activation sites onto metallic 1T-MoS_2 catalysts for enhanced electrochemical hydrogen evolution. *Nat. Commun.* **2019**, *10*, 982. [CrossRef]
3. Niu, H.; Zou, Z.; Wang, Q.; Zhu, K.; Ye, K.; Wang, G.; Cao, D.; Yan, J. Structurally stable ultrathin 1T-2H MoS_2 heterostructures coaxially aligned on carbon nanofibers toward superhigh-energy-density supercapacitor and enhanced electrocatalysis. *Chem. Eng. J.* **2020**, *399*, 125672. [CrossRef]
4. Wang, Y.; Zhang, W.; Guo, X.; Liu, Y.; Zheng, Y.; Zhang, M.; Li, R.; Peng, Z.; Zhang, Y.; Zhang, T. One-step microwave-hydrothermal preparation of NiS/rGO hybrid for high-performance symmetric solid-state supercapacitor. *Appl. Surf. Sci.* **2020**, *514*, 146080. [CrossRef]
5. Cheng, L.; Huang, W.; Gong, Q.; Liu, C.; Liu, Z.; Li, Y.; Dai, H. Ultrathin WS_2 nanoflakes as a high-performance electrocatalyst for the hydrogen evolution reaction. *Angew. Chem. Int. Ed.* **2014**, *53*, 7860–7863. [CrossRef] [PubMed]

6.   Zhuo, S.; Shi, Y.; Liu, L.; Li, R.; Shi, L.; Anjum, D.H.; Han, Y.; Wang, P. Dual-template engineering of triple-layered nanoarray electrode of metal chalcogenides sandwiched with hydrogen-substituted graphdiyne. *Nat. Commun.* **2018**, *9*, 3132. [CrossRef]

7.   Hinnemann, B.; Moses, P.G.; Bonde, J.; Jorgensen, K.P.; Nielsen, J.H.; Horch, S.; Chorkendorff, I.; Nørskov, J.K. Biomimetic hydrogen evolution: MoS$_2$ nanoparticles as catalyst for hydrogen evolution. *J. Am. Chem. Soc.* **2005**, *127*, 5308–5309. [CrossRef]

8.   Yu, X.Y.; Lou, X.W. Mixed metal sSulfides for electrochemical energy storage and conversion. *Adv. Energy Mater.* **2018**, *8*, 1701592. [CrossRef]

9.   Winchester, A.; Ghosh, S.; Feng, S.; Elias, A.L.; Mallouk, T.E.; Terrones, M.; Talapatra, S. Electrochemical characterization of liquid phase exfoliated two-dimensional layers of molybdenum disulfide. *ACS Appl. Mater. Interfaces* **2014**, *6*, 2125–2130. [CrossRef] [PubMed]

10.   Yu, Y.; Nam, G.H.; He, Q.; Wu, X.J.; Zhang, H. High phase-purity 1T′-MoS$_2$ and 1T′-MoSe$_2$-layered crystals. *Nat. Chem.* **2018**, *10*, 638–643. [CrossRef]

11.   Yin, Y.; Han, J.; Zhang, Y.; Zhang, X.; Xu, P.; Yuan, Q.; Samad, L.; Wang, X.; Wang, Y.; Zhang, Z. Contributions of phase, sulfur vacancies, and edges to the hydrogen evolution reaction catalytic activity of porous molybdenum disulfide nanosheets. *J. Am. Chem. Soc.* **2016**, *138*, 7965–7972. [CrossRef]

12.   Yu, X.Y.; Feng, Y.; Jeon, Y.; Guan, B.; Lou, X.W.D.; Paik, U. Formation of Ni-Co-MoS$_2$ nanoboxes with enhanced electrocatalytic activity for hydrogen evolution. *Adv. Mater.* **2016**, *28*, 9006–9011. [CrossRef]

13.   Yu, L.; Xia, B.Y.; Wang, X.; Lou, X.W. General formation of M-MoS$_3$ (M = Co, Ni) hollow structures with enhanced electrocatalytic activity for hydrogen evolution. *Adv. Mater.* **2016**, *28*, 92–97. [CrossRef]

14.   Li, Y.; Zhang, H.; Ming, J.; Yun, K.; Wang, H.; Sun, X. Amorphous Co–Mo–S ultrathin films with low-temperature sulfurization as high-performance electrocatalysts for the hydrogen evolution reaction. *J. Mater. Chem. A* **2016**, *4*, 13731–13735. [CrossRef]

15.   Gao, M.R.; Chan, M.K.Y.; Sun, Y. Edge-terminated molybdenum disulfide with a 9.4-Å interlayer spacing for electrochemical hydrogen production. *Nat. Commun.* **2015**, *6*, 7493. [CrossRef]

16.   Xiao, W.; Liu, P.; Zhang, J.; Song, W.; Feng, Y.P.; Gao, D.; Ding, J. Dual-functional N dopants in edges and basal plane of MoS$_2$ nanosheets toward efficient and durable hydrogen evolution. *Adv. Energy Mater.* **2017**, *7*, 1602086. [CrossRef]

17.   Xie, J.F.; Zhang, H.; Li, S.; Wang, R.X.; Sun, X.; Zhou, M.; Zhou, J.; Lou, X.W. Ultrathin nanosheets with additional active edge sites for enhanced electrocatalytic hydrogen evolution. *Adv. Mater.* **2013**, *25*, 5807–5813. [CrossRef]

18.   Zhang, J.; Wang, T.; Liu, P.; Liu, S.; Dong, R.; Zhuang, X.; Chen, M.; Feng, X. Engineering water dissociation sites in MoS$_2$ nanosheets for accelerated electrocatalytic hydrogen production. *Energy Environ. Sci.* **2016**, *9*, 2789–2793. [CrossRef]

19.   Staszak-Jirkovsky, J.; Malliakas, C.D.; Lopes, P.P.; Danilovic, N.; Kota, S.S.; Chang, K.C.; Genorio, B.; Strmcnik, D.; Stamenkovic, V.R.; Kanatzidis, M.G. Design of active and stable Co-Mo-Sx chalcogels as pH-universal catalysts for the hydrogen evolution reaction. *Nat. Mater.* **2016**, *15*, 197–203. [CrossRef] [PubMed]

20.   Lin, J.; Wang, P.; Wang, H.; Li, C.; Si, X.; Qi, J.; Cao, J.; Zhong, Z.; Fei, W. Defect-rich heterogeneous MoS$_2$/NiS$_2$ nanosheets electrocatalysts for efficient overall water splitting. *Adv. Sci.* **2019**, *6*, 1900246. [CrossRef] [PubMed]

21.   Liu, B.; Yun, W.; Peng, H.Q.; Yang, R.; Zheng, J.; Zhou, X.; Chun-Sing, L.; Zhao, H.; Zhang, W. Iron vacancies induced bifunctionality in ultrathin feroxyhyte nanosheets for overall water splitting. *Adv. Mater.* **2018**, 1803144. [CrossRef] [PubMed]

22.   Zhang, J.; Wang, T.; Pohl, D.; Rellinghaus, B.; Dong, R.; Liu, S.; Zhuang, X.; Feng, X. Interface engineering of MoS$_2$/Ni$_3$S$_2$ heterostructures for highly enhanced electrochemical overall-water-splitting activity. *Angew. Chem. Int. Ed. Engl.* **2016**, *55*, 6702–6707. [CrossRef]

23.   An, T.; Wang, Y.; Tang, J.; Wei, W.; Cui, X.; Alenizi, A.M.; Zhang, L.; Zheng, G. Interlaced NiS$_2$–MoS$_2$ nanoflake-nanowires as efficient hydrogen evolution electrocatalysts in basic solutions. *J. Mater. Chem. A* **2016**, *4*, 13439–13443. [CrossRef]

24.   Tang, Y.; Wang, Y.; Zhu, H.; Zhou, K.; Lan, Y. In situ growth of a POMOF-derived nitride based composite on Cu foam to produce hydrogen with enhanced water dissociation kinetics. *J. Mater. Chem.* **2019**, *7*, 13559–13566. [CrossRef]

25.   Lee, J.E.; Jung, J.; Ko, T.Y.; Kim, S.; Kim, S.I.; Nah, J.; Ryu, S.; Nam, K.T.; Lee, M.H. Catalytic synergy effect of MoS$_2$/reduced graphene oxide hybrids for a highly efficient hydrogen evolution reaction. *RSC Adv.* **2017**, *7*, 5480–5487. [CrossRef]

26.   Wu, L.; Xu, X.; Zhao, Y.; Zhang, K.; Sun, Y.; Wang, T.; Wang, Y.; Zhong, W.; Du, Y. Mn doped MoS$_2$/reduced graphene oxide hybrid for enhanced hydrogen evolution. *Appl. Surf. Sci.* **2017**, *425*, 470–477. [CrossRef]

27.   Xu, J.; Zhang, J.; Zhang, W.; Lee, C.S. Interlayer nanoarchitectonics of two-dimensional transition-metal dichalcogenides nanosheets for energy storage and conversion applications. *Adv. Energy Mater.* **2017**, *7*, 1700571. [CrossRef]

28.   Sun, K.; Zeng, L.; Liu, S.; Zhao, L.; Zhu, H.; Zhao, J.; Liu, Z.; Cao, D.; Hou, Y.; Liu, Y.; et al. Design of basal plane active MoS$_2$ through one-step nitrogen and phosphorus co-doping as an efficient pH universal electrocatalyst for hydrogen evolution. *Nano Energy* **2019**, *58*, 862–869. [CrossRef]

29.   Miao, J.; Xiao, F.X.; Hong, B.Y.; Si, Y.K.; Liu, B. Hierarchical Ni-Mo-S nanosheets on carbon fiber cloth: A flexible electrode for efficient hydrogen generation in neutral electrolyte. *Sci. Adv.* **2015**, *1*, e1500259. [CrossRef]

30.   Kibsgaard, J.; Jaramillo, T.F.; Besenbacher, F. Building an appropriate active-site motif into a hydrogen-evolution catalyst with thiomolybdate [Mo$_3$S$_{13}$]$^{2-}$ clusters. *Nat. Chem.* **2014**, *6*, 248–253. [CrossRef]

31.   Strmcnik, D.; Lopes, P.P.; Genorio, B.; Stamenkovic, V.R.; Markovic, N.M. Design principles for hydrogen evolution reaction catalyst materials. *Nano Energy* **2016**, *29*, 29–36. [CrossRef]

32.   Abdelhamid, A.A.; Yang, X.; Yang, J.; Chen, X.; Ying, J.Y. Graphene-wrapped nickel sulfide nanoprisms with improved performance for Li-ion battery anodes and supercapacitors. *Nano Energy* **2016**, *26*, 425–437. [CrossRef]

33. Kong, D.; Wang, Y.; von Lim, Y.; Huang, S.; Zhang, J.; Liu, B.; Chen, T.; Yang, H.Y. 3D hierarchical defect-rich NiMo$_3$S$_4$ nanosheet arrays grown on carbon textiles for high-performance sodium-ion batteries and hydrogen evolution reaction. *Nano Energy* **2018**, *26*, 425–437. [CrossRef]

34. Chang, K.; Chen, W. L-cysteine assisted synthesis of layered MoS$_2$/graphene composites with excellent electrochemical performances for lithium ion batteries. *ACS Nano* **2011**, *5*, 4720–4728. [CrossRef]

35. Chen, D.; Lin, Z.; Sartin, M.M.; Huang, T.X.; Liu, J.; Zhang, Q.; Han, L.; Li, J.F.; Tian, Z.Q.; Zhan, D. Photosynergetic electrochemical synthesis of graphene oxide. *J. Am. Chem. Soc.* **2020**, *142*, 6516–6520. [CrossRef] [PubMed]

36. Yang, J.; Yu, C.; Hu, C.; Wang, M.; Li, S.; Huang, H.; Bustillo, K.; Han, X.; Zhao, C.; Guo, W.; et al. Surface-confined fabrication of ultrathin nickel cobalt-layered double hydroxide nanosheets for high-performance supercapacitors. *Adv. Funct. Mater.* **2018**, *28*, 1803272. [CrossRef]

37. Ye, J.; Yu, Z.; Chen, W.; Chen, Q.; Ma, L. Ionic-liquid mediated synthesis of molybdenum disulfide/graphene composites: An enhanced electrochemical hydrogen evolution catalyst. *Int. J. Hydrog. Energy* **2016**, *41*, 12049–12061. [CrossRef]

38. Tong, J.; Li, Q.; Li, W.; Wang, W.; Ma, W.; Su, B.; Bo, L. MoS$_2$ thin sheet growing on nitrogen self-doped mesoporous graphic carbon derived from ZIF-8 with highly electrocatalytic performance on hydrogen evolution reaction. *ACS Sustain. Chem. Eng.* **2017**, *5*, 10240–10247. [CrossRef]

39. Zhu, H.; Zhang, J.; Yanzhang, R.; Du, M.; Wang, Q.; Gao, G.; Wu, J.; Wu, G.; Zhang, M.; Liu, B.; et al. When cubic cobalt sulfide meets layered molybdenum disulfide: A core-shell system toward synergetic electrocatalytic water splitting. *Adv. Mater.* **2015**, *27*, 4752–4759. [CrossRef]

40. Zhaojun, L.; Jing, Q.; Moxuan, L.; Shumeng, Z.; Qikui, F.; Hongpo, L.; Kai, L.; Haoquan, Z.; Yadong, Y.; Chuanbo, G. Aqueous synthesis of ultrathin platinum/non-noble metal alloy nanowires for enhanced hydrogen evolution activity. *Angew. Chem.* **2018**, *57*, 11678–11682.

41. Wang, Q.; Shang, L.; Shi, R.; Zhang, X.; Waterhouse, G.I.N.; Wu, L.-Z.; Tung, C.-H.; Zhang, T. 3D carbon nanoframe scaffold-immobilized Ni$_3$FeN nanoparticle electrocatalysts for rechargeable zinc-air batteries' cathodes. *Nano Energy* **2017**, *40*, 382–389. [CrossRef]

42. Tu, Y.; Ren, P.; Deng, D.; Bao, X. Structural and electronic optimization of graphene encapsulating binary metal for highly efficient water oxidation. *Nano Energy* **2018**, *52*, 494–500. [CrossRef]

43. Anjum, M.A.R.; Jeong, H.Y.; Lee, M.H.; Shin, H.S.; Lee, J.S. Efficient hydrogen evolution reaction catalysis in alkaline media by all-in-one MoS$_2$ with multifunctional active sites. *Adv. Mater.* **2018**, *30*, 1707105. [CrossRef]

44. Solomon, G.; Mazzaro, R.; You, S.; Natile, M.M.; Morandi, V.; Concina, I.; Vomiero, A. Ag$_2$S/MoS$_2$ nanocomposites anchored on reduced graphene oxide: Fast interfacial charge transfer for hydrogen evolution reaction. *ACS Appl. Mater. Interfaces* **2019**, *11*, 22380–22389. [CrossRef]

45. Zhao, G.; Lin, Y.; Rui, K.; Zhou, Q.; Chen, Y.; Dou, S.X.; Sun, W. Epitaxial growth of Ni(OH)$_2$ nanoclusters on MoS$_2$ nanosheets for enhanced alkaline hydrogen evolution reaction. *Nanoscale* **2018**, *10*, 19074–19081. [CrossRef]

46. Ojha, K.; Saha, S.; Banerjee, S.; Ganguli, A.K. Efficient electrocatalytic hydrogen evolution from MoS$_2$-functionalized Mo$_2$N nanostructures. *ACS Appl. Mater. Interfaces* **2017**, *9*, 19455–19461. [CrossRef] [PubMed]

47. Zhu, Y.; Song, L.; Song, N.; Li, M.; Wang, C.; Lu, X. Bifunctional and efficient CoS$_2$–C@MoS$_2$ core–shell nanofiber electrocatalyst for water splitting. *ACS Sustain. Chem. Eng.* **2019**, *7*, 2899–2905. [CrossRef]

48. Ibupoto, Z.H.; Tahira, A.; Tang, P.; Liu, X.; Morante, J.R.; Fahlman, M.; Arbiol, J.; Vagin, M.; Vomiero, A. MoSx@NiO composite nanostructures: An advanced nonprecious catalyst for hydrogen evolution reaction in alkaline media. *Adv. Funct. Mater.* **2019**, *29*, 1807562. [CrossRef]

49. Huang, H.; Song, J.; Yu, D.; Hao, Y.; Wang, Y.; Peng, S. Few-layer FePS$_3$ decorated with thin MoS$_2$ nanosheets for efficient hydrogen evolution reaction in alkaline and acidic media. *Appl. Surf. Sci.* **2020**, *525*, 146623. [CrossRef]

50. Diao, L.; Zhang, B.; Sun, Q.; Wang, N.; Zhao, N.; Shi, C.; Liu, E.; He, C. An in-plane Co$_9$S$_8$@MoS$_2$ heterostructure for the hydrogen evolution reaction in alkaline media. *Nanoscale* **2019**, *11*, 21479–21486. [CrossRef]

51. Lin, H.; Li, H.; Li, Y.; Liu, J.; Wang, X.; Wang, L. Hierarchical CoS/MoS$_2$ and Co$_3$S$_4$/MoS$_2$/Ni$_2$P nanotubes for efficient electrocatalytic hydrogen evolution in alkaline media. *J. Mater. Chem. A* **2017**, *5*, 25410–25419. [CrossRef]

52. Lin, C.; Gao, Z.; Jin, J. Boosting alkaline hydrogen evolution activity with Ni-Doped MoS$_2$/reduced graphene oxide hybrid aerogel. *ChemSusChem* **2019**, *12*, 457–466. [CrossRef] [PubMed]